LUND UNIVERSITY

CHARACTERIZING THE ENERGY RESOLUTION OF BLOCH BEAMLINE

Author: Anita Shah

Thesis submitted for the degree of Master of Science

Project duration: 4 months

Supervised by Balasubramanian Thiagarajan

Abstract

The Bloch beamline on 1.5 GeV ring at MAX IV Laboratory is dedicated to measure electronic structure of materials using the technique angle resolved photoelectron spectroscopy (ARPES) and spin resolved photoelectron spectroscopy (spin-ARPES). The main goal of the thesis is to experimentally determine, the energy resolution of the Bloch beamline at 21 eV and 62 eV as a function of the exit slit opening using total ion measurements. To achieve this, one has to first make sure that there was no roll misalignment of the grating. The reason being, if there is a roll misalignment, the beam exiting from the monochromator will move sideways when the grating pitch is changed to choose different energies. This sideway motion has to be then compensated by changing the pitch angle of the optical element after the monochromator.

The first part of the work is to characterize, the pitch change required of the above mentioned optical element after the monochromator as a function of the grating pitch, so the photon beam goes along the correct path. This data was then used to evaluate with a simple model the grating roll error based on the relationship between pitch angle correction of the mentioned optical element and the grating pitch angle. The validity of the model was checked with a ray tracing method before correcting for the grating misalignment. After re-alignment (by the beamline staff), the beam movement was negligible and one could proceed with the experiment to determine the beamline energy resolution at 21 eV and 62 eV using total ion yield measurements.

Populärvetenskapligt sammanfattning

Fotoelektronspektroskopi är ett kraftfullt instrument för materialvetenskap. Det är, av många anledningar, viktigt att känna till hur material fungerar. Denna kunskap kan vi använda för att förstå hur de påverkar och påverkas av miljön runtomkring och för att kunna skapa nya material med bättre egenskaper. Ett exempel på miljöpåverkan är korrosion. För att förhindra korrosion måste man känna till vilka kemiska element materialet innehåller, hur de påverkar varandra och hur de påverkas av miljön de befinner sig i. Korrosion är processer som sker på ytan av ett material och genom att utveckla metoder för analys av ytor hjälper vi ingenjörer att utveckla material med högre resistans mot dessa processer. Fotoelektronspektroskopi är en sådan analysmetod som kan ge information om ytors kemiska komposition och egenskaper.

Fotoelektronspektroskopi baserar sig på den fotoeletriska effekten. En yta bestrålas med fotoner och om de har tillräckligt hög energi kan de sparka ut elektroner, precis som en fotbollsspelare sparkar på en fotboll. Med en analysator och detektor kan man bestämma dessa elektroners kinetiska energi och riktning (fotbollens hastighet). Från den kinetiska energin kan vi beräkna deras bindningsenergi, d v s hur hårt de är bundna till materialet, ungefär som gravitationskraften mellan jorden och oss. Bindningsenergin kan ofta användas för att identifiera de kemiska elementen i materialet. Från riktningen kan vi beräkna elektronernas rörelsemängd vilket ger information om t ex elektriska och magnetiska egenskaper.

För att bestämma om en yta beter sig som en metall eller som en halvledare studerar vetenskapsmän den så kallade elektroniska bandstrukturen. En ytas egenskaper, så som elektrisk och termisk ledningsförmåga, magnetism, m m (d v s hur de beter sig i den miljö de befinner sig i) är direkt relaterade till bandstrukturen. Ett exempel är grafen – världens tunnaste elektriskt ledande material – som inte har ett gap mellan valens- och ledningsband. Genom att t ex tillföra andra material eller skapa grafen nano ribbons kan vi öppna upp ett gap och skapa en halvledare som kan användas av elektronikindustrin. I framtiden har kanske grafenbaserad elektronik helt ersatt kiselbaserad elektronik. Med vinkelupplöst fotoemission kan man direkt mäta den elektroniska bandstrukturen (sambandet mellan energi och rörelsemängd) och är därför en kraftfull teknik för att t ex hitta bandgap.

Den totala energiupplösningen är summan av bl a upplösningen i fotonenergin och upplösningen i elektronanalysatorn. Det är viktigt att varje bidrag till den totala upplösningen är så litet så möjligt. Mitt bidrag är att karaktärisera upplösningen i fotonenergin.

Contents

List of Figures

List of Tables

1   Acronyms

EPU	Elliptically Polarized Undulator
PGM	Plane Grating Monochromator
PG	Plane Grating
CPGM	Collimated Plane Grating Monochromator
ARPES	Angle-Resolved Photoelectron Spectroscopy
Spin-ARPES	Spin-Angle Resolved Photoelectron Spectroscopy
PES	Photoelectron Spectroscopy
XPS	X-ray Photoelectron Spectroscopy
CLS	Core-Level Spectroscopy
FWHM	Full Width Half Maximum
UV	Ultra Violet

2 Introduction

The Bloch beamline with its two branchlines is situated on the 1.5 GeV ring at MAX IV laboratory and is utilised to perform a broad range of investigation especially connected to materials [1] . The focus of the beamline is to perform ARPES, Spin-ARPES and shallow CLS [1]. The source for the beamline is the photons produced by the electrons moving through the Elliptically Polarized Undulator (EPU). Using a grating (monochromator), the photons with different energies are separated from each other, allowing the selection of a monochromatic photon beam using an exit slit. This beam is then focused onto a sample at ARPES or Spin-ARPES end station.

The end station consist of a large hemispherical analyzer with a 2-D detector. The photons from the beamline interact with the surface of sample and cause the emission of photo-electrons, which is known as photoelectric effect. The spectroscopy based on this is referred as Photon Electron Spectroscopy (PES). The photo-electrons emitted from the sample at various kinetic energies and angles, pass through a hemispherical electron analyzer and are detected by a 2D detector. The hemispherical analyzer consists of various electrostatic lenses, followed by entrance slit, two electrostatic concentric hemispheres and finally a 2D detector. The lenses focus the electrons on the entrance slit of the concentric hemispheres. To measure electrons of a specific kinetic energy, the voltages on the lenses are set such that the required kinetic energy is either retarded or accelerated to the pass energy of analyzer. The hemispheres act as energy filtering device. The combination of pass energy, slit width and the mean radius of the hemispheres determine the energy resolution of the electron analyzer. By scanning the lens voltages, one can measure different kinetic energies. Apart from the kinetic energy, one can also measure the angles along the non-dispersive direction of the hemispheres. From the kinetic energy and the angle at which the electron emitted, one can find parallel component of momentum and binding energy of the electrons. The relationship between momentum and binding energy of the electron is called electronic band structure in solids (electronic structure is more general).

Using conservation of the total energy, the relationship between the kinetic energy of the outgoing electrons and photon energy is given by

$$E_K = h\nu - (E_B + \phi) \tag{1}$$

where E_K is kinetic energy, ϕ is work function and E_B is binding energy. From the above relation, one can find the binding energy of an electron inside the sample. X-ray Photoelectron Spectroscopy (XPS) is a versatile tool for understanding material. In XPS, one plots intensity of photo-electrons versus its kinetic energy. From the kinetic energy, one can find the binding energy. Since the binding energy is a fingerprint of the element, the spectrum gives the presence of different elements in the sample. One can

also determine the chemical state of element, that is whether it is oxidized or neutral. Apart from the peak position of spectra which gives the binding energy, the peak width is also important parameter and gives information about the life time of the core-level. For quantitative interpretation of the XPS spectra, one needs to have good energy resolution for both analyzer and photons. For example, in some of the cases like, small spin-orbit splitting, small surface to bulk core-level shift or two different elements having close binding energies, the spectra will contain two or more peaks which are close by. If the energy resolution of photons or the analyzer is larger than the binding energies between these peaks, one would not be able to resolve them. To show the effect of photon energy resolution, one can make a simple model of two closely spaced Gaussian core-levels with energy distribution centered around their respective binding energies as shown in Figure 1. The red curve in the Figure shows with zero energy resolution of photon. The parameters used for the red curve in Gaussian distribution are standard deviation $\sigma_1 = \sigma_2 = 0.005\,\text{eV}$ (include broadning due to life time and also due to energy resolution of the electron analyzer). The binding energies are chosen to be 100 and 100.02 eV. The blue curve is a convoluted spectra assuming Gaussian distribution of the photons with energy resolution (FWHM) of 0.02 eV ($\sigma_p = 0.0085\,\text{eV}$). It should be mentioned that if only He lifetime broadening is considered, core-levels typically have Lorentzian line shape or if thermal broadening is included, a Voigt line shape. The Gaussian model is used here only for demonstration purpose, as it simplifies the convolution procedure. Convolution of two Gaussians with standard deviation σ_a and σ_b gives a Gaussian with $\sigma = \sqrt{\sigma_a{}^2 + \sigma_b{}^2}$.
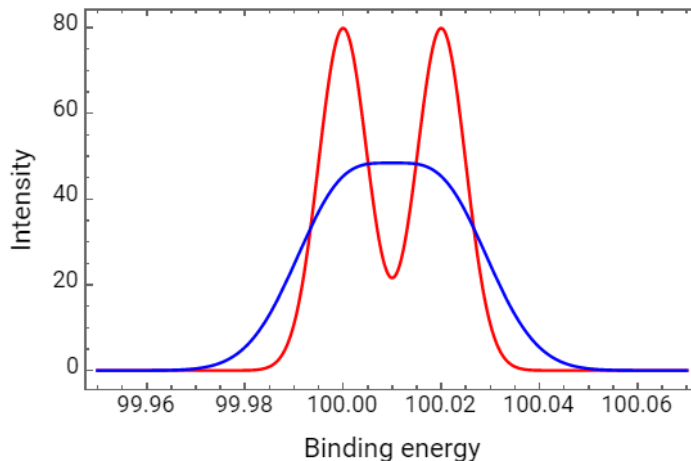
Figure 1: In graph, the red line shows two close peaks of core-level (assuming Gaussian shape). The blue line shows same but convoluted with Gaussian photon energy resolution. From blue line, it is clear that the two peaks are not clearly resolved.

Many properties of materials like electrical conductivity, superconductivity, magnetism etc, are closely related to its electronic band structure (relationship between energy and momentum of the electron inside the material) ARPES is a direct tool to measure the

electronic band structure.

For electronic band measurements, apart from binding energy, one also need to measure the momentum of electron. The kinetic energy and momentum relation for electron outside the sample is

$$E_k = \frac{\hbar^2 k^2}{2m} \tag{2}$$

From the above equation, the magnitude of momentum of the electron outside the solid is

$$k = \sqrt{\frac{2m}{\hbar^2}} \cdot \sqrt{E_k} \tag{3}$$

From the above equations, one can infer that any uncertainity in the measurement of the kinetic energy (either from the energy resolution of analyzer or photon) will create uncertainty in momentum. There are two components of momentum, one is parallel and another is perpendicular component. The perpendicular component of the momentum is not conserved due to change in the potential perpendicular to the sample. However, the parallel component is conserved. The parallel component ($k_{||}$) of momentum outside the solid can be determined from

$$k_{||} = \sqrt{\frac{2m}{\hbar^2}} \cdot \sqrt{E_k} \sin \theta \tag{4}$$

where θ is the angle of emission of electron from the surface normal. Hence, different $k_{||}$ can be measured by detecting electrons at different angles coming out from sample. This is true assuming that the photon has not transferred any momentum to the electron. For energies at which ARPES is performed on Bloch (E $<$ 200 eV), the electron momentum is about 100 times or more than photon momentum. To show the effect of photon energy resolution on the electronic band structure, one can model a free electron in conduction and valence bands, split with a small band gap. Similar to the core-level modelling, for demonstration purposes, one can use a Gaussian distribution in energy. However, here the binding energy changes with $k_{||}$ and hence the Gaussian distribution will be a function of two variables. The high energy resolution is necessary to measure the band gap are shown in Figure 2. The parameters used for the Figure 2a, are standard deviation $\sigma_1 = \sigma_2 = 0.003$ eV (includes broadening due life time as well as the energy resolution of the electron analyzer) and a band gap of 0.015 eV. The Figure 2b is a convoluted image assuming Gaussian distribution of the photons with energy resolution (FWHM) of 17 meV.

| (a) | (b) |
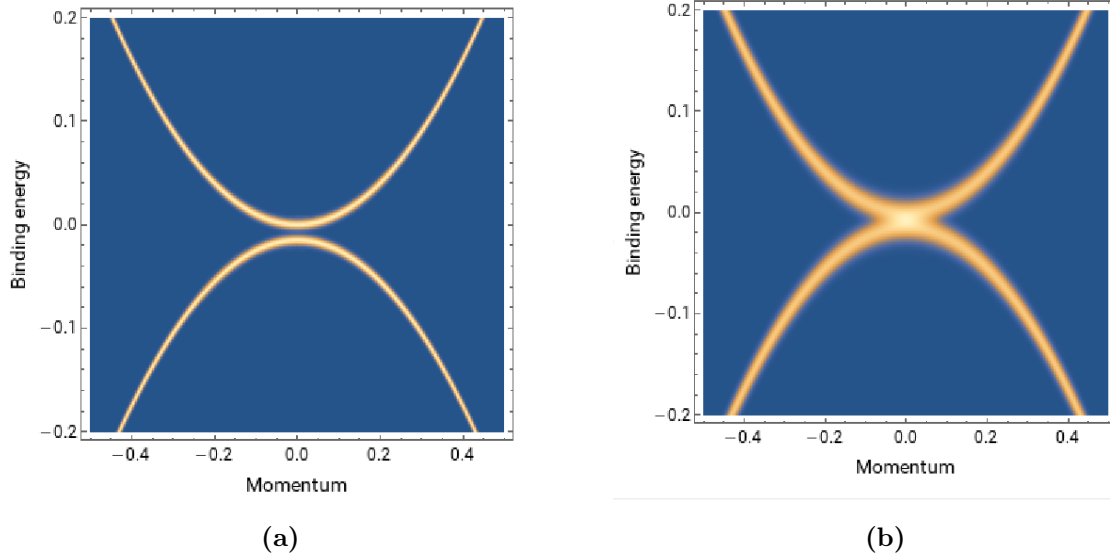
Figure 2: The left panel shows two free electron like conduction and valence bands, assuming Gaussian energy distribution for every momentum. The right panel shows the same but convoluted with energy resolution of the photons. It is clear from right panel that band gap is not clearly visible.

These simple models for both in XPS and ARPES show that, characterizing and optimizing the beamline energy resolution is important. This is one of the motivation of this work.

3   Background

3.1   Undulator

An undulator consists of a periodic structure of magnets and is placed on a straight section between bending magnets in a synchrotron storage ring. An illustration of an undulator is shown in Figure 3.
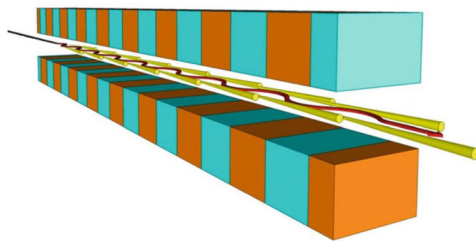
Figure 3: Image shows how the undulator produces photons (yellow) from electrons (red colour) when they are passing through dipole magnets that are arranged perpendicular to the direction of electron flow. This image taken from [2].

An electron passing through an undulator, oscillates due to the periodic magnetic field

inside this undulator. The radiation produced by the electron can be characterized by the dimensionless parameter K.

$$K = \frac{e}{2\pi mc}\lambda_u B, \tag{1}$$

where B is the magnetic field, e is electron charge, m is mass of an electron, c is the speed of light and λ_u is the period length of the undulator.

The dimensionless parameter K is proportional to the amplitude of electron oscillation. If K is much larger than 1, the oscillation amplitudes are large, the radiation produced from each bend adds up independently and generates broad energy spectrum. The insertion device is called a wiggler. If K is around 1, oscillation amplitudes are small and the radiation produced from each bend constructively interfere producing a narrow spectrum of wavelength λ, given by:

$$\lambda = \frac{\lambda_u}{2\gamma^2}(1 + \frac{K^2}{2} + \gamma^2\theta^2) \tag{2}$$

where θ is angle from the axis of an undulator and γ is the Lorentz factor of electron defined as $\gamma \approx \sqrt{(1 - \frac{v^2}{c^2})}$. This kind of device is called an undulator. The above equation shows that the fundamental wavelength λ depends on K^2 which in turn depends on magnetic field. The magnetic field can be varied by changing the undulator gap i.e. the distance between upper and lower set of magnets. Hence various λ (energy) can be produced by changing the undulator gap. The typical central cone ($\theta \approx 0$) undulator spectra from Bloch at different gap or equivalently at different K values are shown in Figure 4.
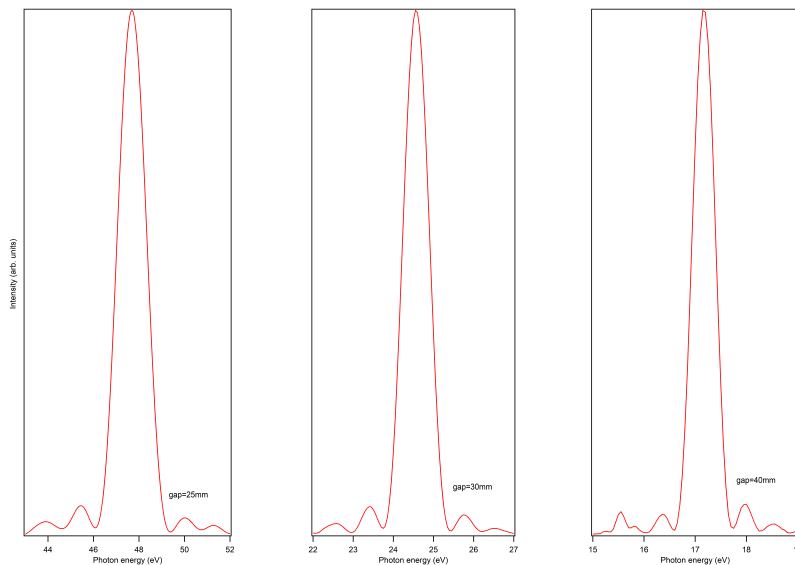
Figure 4: Undulator spectra at different gap.

3.2 Toroidal mirror

Mirrors have different geometric shape, their optical surface can be planar, toroidal, spherical, paraboloidal, ellipsoidal and can be used for different purpose. In a beamline, mirrors play vital role in focusing and changing the direction of photons. Toroidal mirrors are commonly used and have two different radii whose axes are oriented perpendicularly see Figure 5 [3]. The tangential plane (deflection plane) contains central incident ray (having long radius R) and sagittal plane (having small radius r) is a plane perpendicular to tangential plane. Principal diagram of toroid mirror is as shown in Figure 5
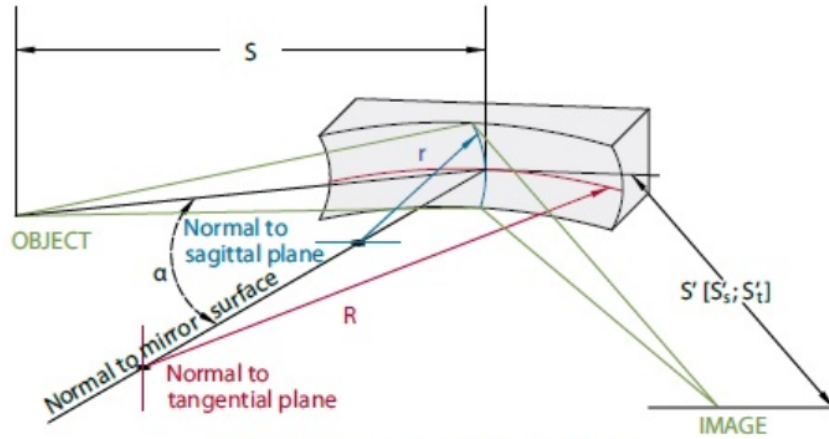
Figure 5: Toroidal mirror focuses horizontally and collimate vertically at the same distance S' in beamline [3].

Toroid focusing equations are

$$\frac{1}{S} + \frac{1}{S'_s} = \frac{2\cos\alpha}{r} = \frac{1}{f_{sag}} \tag{3}$$

$$\frac{1}{S} + \frac{1}{S'_t} = \frac{2}{R\cos\alpha} = \frac{1}{f_{tan}} \tag{4}$$

where α is the angle of incidence measured relative to normal.
S and S' are object and image conjugate distances in general and
S'_s and S'_t are distances to sagittal and tangential foci, respectively.
Here, r and R are radius in sagittal and tangential plane respectively.
As an example to show the focusing property of a toroidal mirror for $\alpha = 87°$, radius r = 1465.4mm, R = 246 925.4 mm, S = 14 000 mm which are the parameters for the first mirror of Bloch. Using these parameters in the Equations 3 and 4, the sagittal image distance is infinity (i.e. light is collimated) and tangential image distance is 12 000 mm.

The graph below presents the sagittal image position as a function of the angle of incidence, showing the collimation is very sensitive to the angle of incidence.
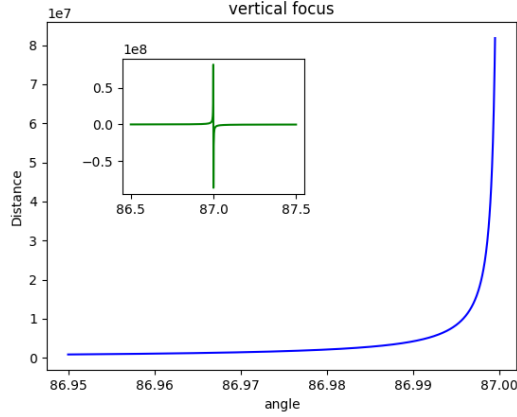
Figure 6: Variation of the sagittal image distance with the angle of incidence of toroid mirror. Inset shows at wider angle range.

3.3 Plane grating

Plane grating is an artificial periodic structure with a well defined period, d, equivalently $(N = 1/d)$, where $N =$ line density. If α and β are the grazing angle of incidence and diffraction, then the wavelength λ of the diffracted beam of order, m, is given by

$$\lambda = \frac{1}{Nm}(\cos\alpha - \cos\beta) \tag{5}$$
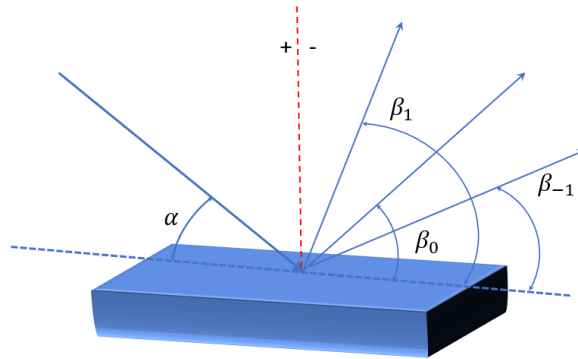
Figure 7: Diffraction beam at grazing incident angle α. β_0, β_1 and β_{-1} are the diffracted angles at zero order (m = 0) and first orders (m = 1 and -1) respectively using Equation 5.

3.4 Rydberg and autoionization state

High lying excited states very close to the ionisation threshold are called Rydberg states. Their energies are closely spaced and converge to the ionisation energy of electrons in the most outer shell. The closer to the ionisation threshold, the closer is the spacing between the Rydberg states. A process of exciting one of the outer-shell electron from neutral

state to a ionized state is called auto-ionization. Therefore exciting the electron to the Rydberg states, one can auto-ionise the atom.
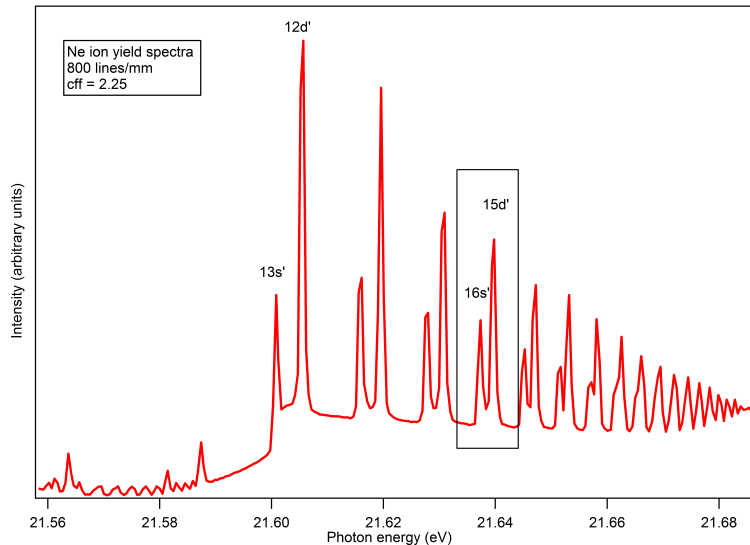
Figure 8: The total ion yield spectrum of neon, obtained at $100\,\mu m$ slit width with $800\,$lines/mm.

The fact that Rydberg states are energetically closely spaced (and their spacing decreases when approaching to the ionisation threshold) can be used to estimate the energy resolution beamline. Furthermore, the energy width of these excited states are typically in the microvolts to millivolts regime. Hence it can be a useful tool to characterize the energy resolution. For example, Neon in ground state has an electron configuration $1s^2 2s^2 2p^6$. The ionisation threshold for $2p^{3/2}$ electron of Ne is about $21.56\,$eV and $2p^{1/2}$ is about $21.66\,$eV. A series of auto-ionizing states (s and d – Rydberg states) exist below these two thresholds. Photon energy resolution can be estimated either by counting the number of resolvable states or measuring their line widths. Since the natural line widths of these states are below $0.1\,$meV, they can also be used to estimate the beamline energy resolution [4]).

Another example is autoionisation states of doubly excited He. These lie in energy range between 60 - 80 eV and have several narrow line widths (less than $0.1\,$meV) and can be used for estimating beamline energy resolution [5].

4 Optical design of Bloch Beamline

The Bloch beamline on 1.5 GeV ring at MAX IV Laboratory is dedicated for measuring electronic structure of materials by high resolution ARPES and Spin-ARPES. The detailed design report of the beamline is described in Ref [1]. The beamline is sourced by a $84\,$mm period and $2.6\,$m long quasi- periodic elliptically polarising undulator. The photon energies of Bloch beamline range from UV (10 eV) up to soft X-ray region (1000 eV). In

order to achieve high flux and high energy resolution for typical ARPES measurements, special attention is given for energies below 200 eV [1]. The beamline has two branchlines, one dedicated for ARPES and other spin-ARPES.

The optical layout of Bloch beamline is shown in Figure 9.
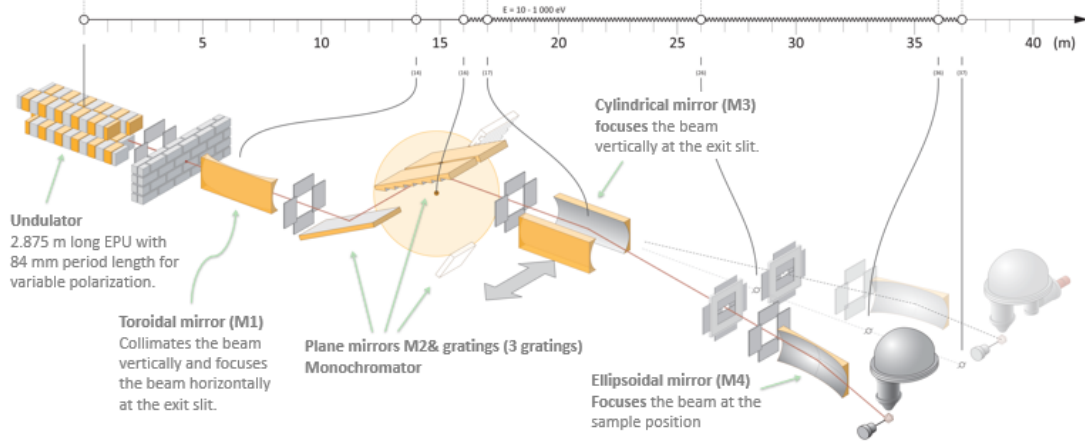
Figure 9: Optical layout showing various optical component and corresponding distances of a beamline. The switching mirror M3 allow one to choose ARPES and Spin-ARPES branch line. The schematic image was taken from [6].

The first optical element in the beamline is a toroidal mirror, M1, situated at 14 m from the undulator. M1 collimates the beam vertically and focuses the beam horizontally at the exit slit which is 12 m away from M1. The vertically collimated beam passes through a monochromator, which consist of a plane mirror, M2, and a Plane Grating (PG). The above mentioned setup is called CPGM. The distance between M1 and PG is 2 m. The energy dispersed beam from the grating in the vertical plane is focused by a cylindrical mirror, M3, at the exit slit. The distance between M3 and the monochromator is 1m and the distance between M3 and the exit slit is 9m. The combination of horizontal focus by M1 and vertical focus by M3 provides a stigmatic when beam is focussed at the exit slit e.g.(i.e. horizontal and vertical focus are at the same place). Finally, an ellipsoidal mirror, M4, focuses the beam at the end station. The distance between the exit slit and M4 is 10 m and between M4 and the end-station (sample position) is 1m. These gives the de-magnification factor of 10:1. Hence for an exit slit opening of 100 x 100 µm, the spot size at sample position would be 10 x 10 µm. The optical parameters of the beamline are shown as Table 1.

The performance of beamline depends on the alignment of the optical elements. The first topic in this project is to investigate the effect of roll misalignment of the grating. This is done by an analytical model and a ray tracing model. The results and the concepts from these models are then used to estimate and correct the roll misalignment experimentally. Another important quality of the beamline is the energy resolution, and it is the second topic of investigation. This is done by an analytical model and a full ray tracing model of

Table 1: Parameters of the optical elements at the Bloch Beamline [1].

Optical element	M1	M2	Grating	M3	Exit slit	M4
Shape	toroid	plane	Plane	cylinder	rectangle	ellipsoidal
Deflection	horizontal	vertical	vertical	horizontal	-	horizontal
Incident angle	$3°$	$0° - 21°$	$0° - 30°$	$3°$	-	$3°$
Opt. size (mm)	340x20	570 x 15	15 x 136	200 x 60	adj.	200 x 60
Entrance arm(mm)	14000	-	-	$-/\infty$	-	10000
Exit arm(mm)	$12000/\ \infty$	-	-	$-/9000$	-	1000
Parameters (mm)	$R = 246925.4$ $\rho = 1465.4$	-	-	$\rho = 942.05$	$0 - 4\,\mathrm{mm}$ $0 - 50\,\mathrm{\mu m}$	36000

beamline. Finally, ion yield experiments are performed using a gas cell mounted after the exit slit. These results are then compared with analytical as well as ray tracing models.

5 Grating roll alignment

5.1 Analytical method

As mentioned above, assuming that M2 is perfectly aligned and also that the grating is kept at the same angle as M2 in the monochromator (zero order condition). A simple model be derived using just two plane mirrors as shown in Figure 10a, mirror 1 mimics the grating and mirror 2 mimics M3.

(a)	(b)
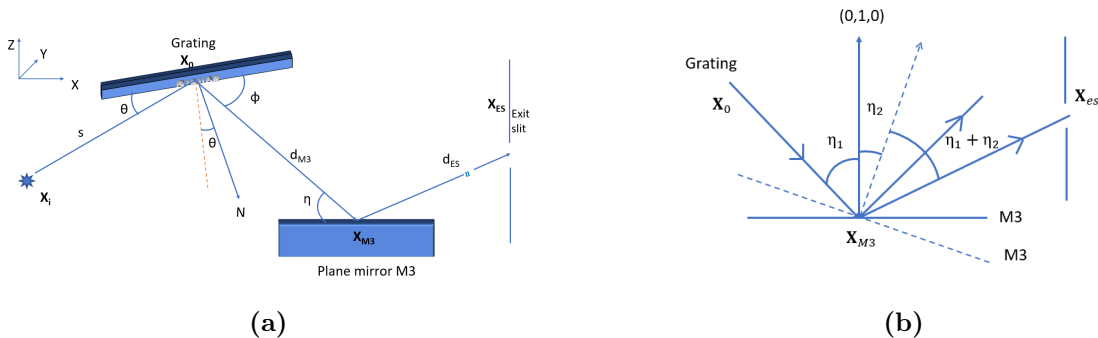
Figure 10: The left panel shows a sketch of the set up used for analytical model defining the various angles and elements used. The right panel shows a sketch defining angles $\eta 1$ and $\eta 2$

.

Before starting to find the effect of roll misalignment on grating, it is important to

derive the 3D-reflection formula .

$$\mathbf{x_r} = -\mathbf{x_i} + [2(\mathbf{x_i} - \mathbf{x_0}) \cdot \hat{N}]\hat{N} + 2\mathbf{x_0} \tag{1}$$
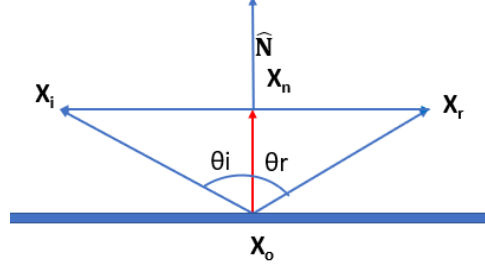
Figure 11: Figure showing the law of reflection.

To derive, it is important to understand the law of reflection on plane mirrors as shown in Figure 11. (1) The incident ray $\mathbf{x_i}$, the reflected ray $\mathbf{x_r}$, and the normal $\hat{N}$ to the surface of the mirror all lie in the same plane. (2) The angle of reflection is equal to the angle of incidence. From Figure 11, the projection of $\mathbf{x_i}$ along $\hat{N}$ is given by

$$\mathrm{proj}_{\vec{N}}(\mathbf{x_i}) = (\mathbf{x_i} - \mathbf{x_0}) \cdot \hat{N} \tag{2}$$

Position of $\mathbf{x_n}$ with respect to $\mathbf{x_0}$ is

$$\mathbf{x_n} = \mathbf{x_0} + [(\mathbf{x_i} - \mathbf{x_0}) \cdot \hat{N}]\hat{N} \tag{3}$$

According to the law of reflection,

$$\mathbf{x_i} - \mathbf{x_n} = \mathbf{x_n} - \mathbf{x_r} \tag{4}$$

$$\mathbf{x_r} = \mathbf{x_i} + 2\mathbf{x_n} \tag{5}$$

Therefore, substituting equation 3, the reflected ray $\mathbf{x_r}$ direction is

$$\mathbf{x_r} = -\mathbf{x_i} + [2(\mathbf{x_i} - \mathbf{x_0}) \cdot \hat{N}]\hat{N} + 2\mathbf{x_0} \tag{6}$$

which is the desired 3D-vector reflection formula.

As shown in Figure 10a, the light from the point source whose position is $\mathbf{x_i} = (0,0,0)$ is incident on grating placed at $\mathbf{x_0} = (s,0,0)$. For a pitch $\theta = 0$, the unit vector normal to the grating would be $\hat{N} = (0, 0,-1)$. Assuming that, there was a roll misalignment angle ϕ of the grating. Then the normal vector $\hat{N}_g$ for any pitch angle θ will be $R_\theta \cdot R_\phi \cdot \vec{N}$ ($\hat{N}_g$ derivation is shown in the Appendix A-7), where R_θ and R_ϕ are rotation matrices.

$$\hat{N}_g = (-\cos\phi\sin\theta, -\sin\phi, -\cos\theta\cos\phi) \tag{7}$$

Using equation 6, the reflected ray from the grating will now have for coordinates

$$\mathbf{x_r} = (2s(1 - \cos^2 \phi \sin^2 \theta), -s \sin 2\phi \sin \theta, -s \cos^2 \phi \sin 2\theta) \tag{8}$$

If the roll and/or the pitch of the grating and/or not zero, it can be seen from the Y coordinate of the reflected beam after the grating. It will not reach the exit slit. One can adjust the mirror M3 to reflect the beam back to the exit slit. The task is then to find the angle of M3 to bring back the beam to the exit slit. The unit vector from $(\mathbf{x_0}$ to $\mathbf{x_r})$ is $(\mathbf{x_r} - \mathbf{x_0})/\sqrt{(\mathbf{x_r} - \mathbf{x_0}) \cdot (\mathbf{x_r} - \mathbf{x_0})}$. If d_{M3} is the distance between grating and M3, the position of $\mathbf{x_{M3}}$ M3 would be given by

$$\mathbf{x_{M3}} = \mathbf{x_0} + d_{M3}(\mathbf{x_r} - \mathbf{x_0})/\sqrt{(\mathbf{x_r} - \mathbf{x_0}) \cdot (\mathbf{x_r} - \mathbf{x_0})} \tag{9}$$

which in terms of coordinates M3 is

$$\mathbf{x_{M3}} = (s + d_{M3}(1 - 2s(1 - \cos^2 \phi \sin^2 \theta), -d_{M3} \sin 2\phi \sin \theta, -d_{M3} \cos^2 \phi \sin 2\theta)) \tag{10}$$

If the grating has a roll of ϕ, the angle of incidence $\eta 1$ on M3 with respect to the normal $(0, 1, 0)$ is

$$\eta_1 = acos((\mathbf{x_r} - \mathbf{x_0})/\sqrt{(\mathbf{x_r} - \mathbf{x_0}).(\mathbf{x_r} - \mathbf{x_0})} \cdot (0, 1, 0)) \tag{11}$$

$$\eta 1 = acos(sin2\phi sin\theta) \tag{12}$$

For small angles of ϕ and θ, we can assume, and $sin2\phi \approx 2\phi$, $sin\theta \approx \theta$. Using $acos(x) \approx \pi/2$-x for small x, one obtains

$$\eta_1 = \frac{\pi}{2} - 2\phi\theta \tag{13}$$

On Bloch beamline, the distance between M3 and the exit slit is 9 times larger than the distance between the grating and M3. Hence the reflected beam from M3 will not go in the direction of the exit slit (see right panel of Figure 13.)

Let η_2 be the angle by which the normal of M3 along $(0, 1, 0)$ has to be rotated to bring back the beam to the exit slit, then the new M3 normal $\widehat{N}_{M3}$ can be written as

$$\widehat{N}_{M3} = (\sin \eta 2, \cos \eta 2, 0) \tag{14}$$

If d_{ES} is the distance between M3 and the exit slit, the position of the exit slit can be determined

$$\mathbf{x_{ES}} = \mathbf{x_{M3}} + d_{ES}(\mathbf{x_{M3}} - \mathbf{x_0})/\sqrt{(\mathbf{x_{M3}} - \mathbf{x_0}).(\mathbf{x_{M3}} - \mathbf{x_0})} \tag{15}$$

The y-coordinate of the reflected beam after the exit slit can then be written as

$$(d_{M3} + d_{ES}) \cos \phi \sin \phi \sin \theta + d_{ES} \cos \eta_2(-\cos \eta_2 \sin 2\phi \sin \theta + \sin \eta_2)$$
$$-d_{ES} \cos^2 \phi \sin^2 \theta \sin 2\eta_2 \tag{16}$$

Choosing the proper η_2 value for M3, one can bring back the beam at exit slit. The value for η_2 can be obtained by solving the equation below.

$$(d_{M3} + d_{ES}) \cos \phi \sin \phi \sin \theta + d_{ES} \cos \eta_2 (- \cos \eta_2 \sin 2\phi \sin \theta + \sin \eta_2)$$
$$-d_{ES} \cos^2 \phi \sin^2 \theta \sin 2\eta_2 = 0 \tag{17}$$

For small angles θ, ϕ and η_2, using $cosx \approx 1, sinx \approx x$ and $sin^2 x \approx 0$, then,

$$(d_{M3} + d_{ES})(\phi\theta) + d_{ES}(-2\phi\theta + \eta_2) = 0 \tag{18}$$

$$\eta_2 = (\frac{d_{ES} - d_{M3}}{d_{ES}})\phi\theta \tag{19}$$

The final normal incidence angle on M3 to send the beam in the direction of the exit slit, will be $\eta_1 + \eta_2$

$$\eta_1 + \eta_2 = \frac{\pi}{2} - 2\phi\theta + (\frac{d_{ES} - d_{M3}}{d_{ES}})\phi\theta \tag{20}$$

The grazing incidence angle would finally be $\pi/2$-$(\eta_1 + \eta_2)$,

$$\eta = (\frac{d_{ES} + d_{M3}}{d_{ES}})\phi\theta \tag{21}$$

This says that within the small angle approximation, for a given roll misalignment, the incident angle on M3 is linear with the grating pitch angle. The slope is proportional to the roll misalignment of the grating. One can also see that when $d_{M3} = d_{ES}$, $\eta = 2\phi\theta$, as expected. One can also notice that if $d_{ES} >> d_{M3}$, the slope will be very close to the roll misalignment. For the parameters of the bloch beamline ($d_{ES} = 9$ and $d_{M3} = 1$), the roll misalignment is 0.9 times slope of M3 versus grating pitch plot.

It is important to mention that, in this simple analytical model, one has translated M3 from its original position with no roll on the grating. If one does not translate M3, the reflected beam from the grating with a roll will not reach M3. The translation is done in such a way that absolute distance between the grating and M3 along the beam path is same as the distance without roll. This assumptions seems to be valid in the small angle approximation. The results from the analytical model was checked using a ray tracing model in the next section and agrees reasonably well.

5.2   Ray tracing method

In 1984, a ray tracing program RAY was started for ray tracing calculations of VUV- and soft X-ray optical schemes at BESSY [7]. In RAY, all the options for selecting different source (point source, undulator,...), grating (plane, spherical,...) and also optical element like mirrors (plane, cylindrical, spherical....), are available to build a beamline model. It is easy to setup intensity, energy, energy spread of the light source, that generate a set of rays passing through all optical elements and finally display at the exit slit result, for example Figures 13. Even slope errors, misalignment, incident angle, radius of curvature can be adjusted as per geometry of beamline on mirrors. In order to collect data, a screen

(exit slit, aperture...) is inserted at any position of the beamline allowing to visualize the properties like intensity, angular distribution, pathlength and the energy resolution.

5.2.1 Simulation of the effect of grating roll misalignment

The model which is set up using RAY software in Figure 12 and follows very close to the Bloch beamline setup, except that the grating is replaced by a plane mirror PM2. The model contains simple undulator generating a set of beam of 20000 rays propagating per run. The beam direction is along the Z-axis from undulator which is then incident on next optical component that is toroid mirror. The toroid is kept at 90° azimuthal angle with respect to beam direction. Like on the Bloch beamline, the toroid collimates the beam in vertical plane and focuses in the horizontal at the exit slit. Next there are two plane mirrors PM1 and PM2 which are at 0° and 180° azimuthal angle with respect to the beam direction respectively. PM2 is setup with a chosen roll of 10 mrad which mimics the roll misalignment of the grating. Later, the cylindrical mirror (M3 mirror) is kept at 90° azimuthal angle, whose purpose to focus the vertical beam on the exit slit. The exit slit aperture having dimension (200 x 200 mm) is set to observe the output footprint of reflected beam spot.
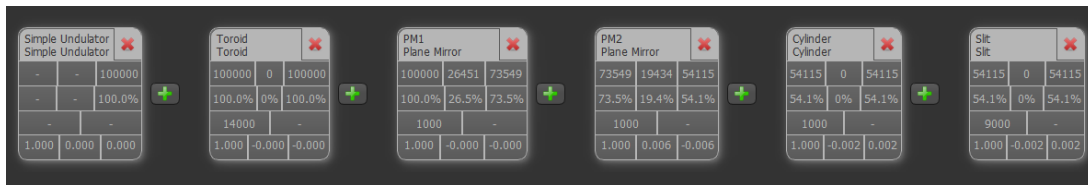
Figure 12: Optical elements for studying grating roll misalignment in ray tracing software "RAY"

By changing the angle of incidence on PM1 and PM2 simultaneously and since PM2 has fixed roll, the beam moves away from the center of exit slit as in Figure 13a. By choosing a proper pitch angle of the cylindrical mirror, one can bring back the beam to the center of the exit slit as shown in Figure 13b.

Ray tracing results for various pitch angle of PM2 (PM2=PM1) versus cylindrical mirror (M3) for a roll misalignment of 10 mrad is shown in Figure 14. The graph is linear in the plotted range. The slope of cylindrical mirror to the plane mirror pitch angle is obtained by a linear fit and is 10.998 mrad. This means, the set roll misalignment is about 0.909 times the slope. In the small angle approximation of the simple analytical model (see Eq. 19), the slope is 0.9 times the roll misalignment angle which is quite close to value obtained through ray tracing.

(a)

(b)
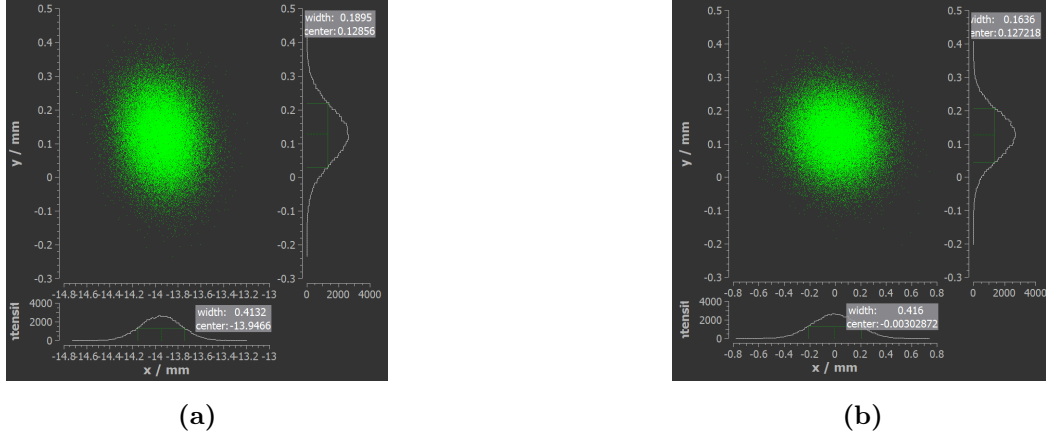
Figure 13: (a) The beam at the exit slit moved away from the centre by -13.9466mm after simulation: the rotation roll on PM2 $= 10$ mrad and the grazing incident angle on PM1 and PM2 $= 4°$. (b) The beam of intensity back to the centre by rotating the pitch angle $\eta = 0.775$ mrad of the the cylindrical mirror (M3).
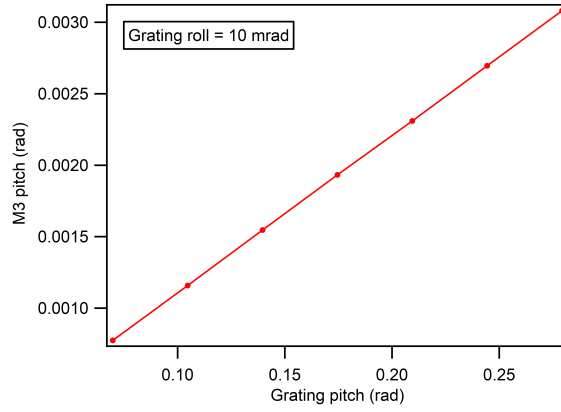
Figure 14: Ray tracing results of the grating (PM2) versus M3 pitch angles to bring back the beam to the exit slit for PM2 roll misalignment of 10 mrad. The slope from linear fit is 10.998 mrad, which is about 0.909 times the roll misalignment. The data used to plot the Figure is shown in Table 2.

Table 2: Data obtained from ray tracing method for a grating roll misalignment of 10 mrad.

Grating pitch angle (°)	Grating pitch angle (rad)	(η) angle (rad)	slope
4	0.0698	0.000775	
6	0.1047	0.0011589	
8	0.1396	0.00154627	Linear Fit
10	0.1745	0.0019328	0.010998 $\pm$0.000015
12	0.2094396	0.00230998	
14	0.2443462	0.00269497	
16	0.2792528	0.00307996	

6 Energy resolution

6.1 Analytical method

The derivation used in this section closely follow references [8] and [9]. The basic concept of the beamline in Petersen geometry is shown in Figure 15. Petersen geometry was first introduced by Petersen in 1982 [10]. In this geometry, the source having size,S, is kept at a distance R from the deflecting mirror,M2, (where the reflected beam), is incident on a plane grating. The cylindrical mirror, M3, which is at distance,D, from the grating, focuses the beam at the exit slit placed at a distance R''. To change the energy, one then rotates both, M2 and the grating in such a way that the total deflection angle from M2 is same as the total deflection angle from the grating. That is twice the angle of incidence on M2 should be equal to incidence plus diffraction angle of the grating. The virtual
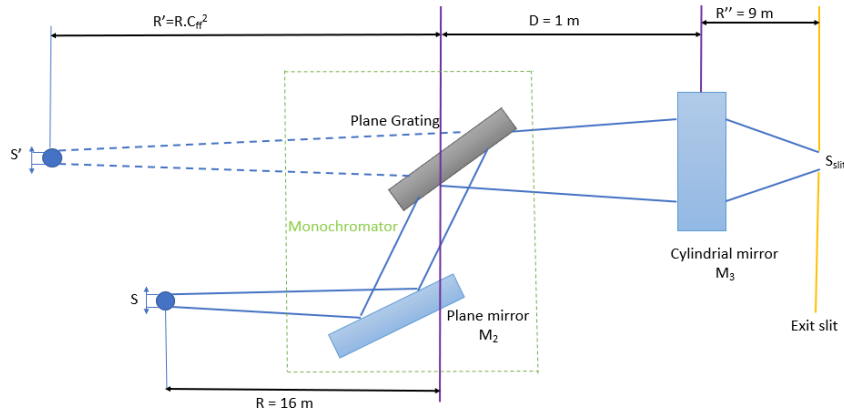
Figure 15: Optical layout of PGM shows virtual image by dotted blue lines

image S' formed by the grating at a distance R' from centre of the grating, now becomes

the source for cylindrical mirror M3. The orientation of the mirror M2 and the grating are arranged in such a way that, the reflected beam will always focus at the exit slit.

Using the optical path function and Fermat's principle, one can analyze the focusing property of a plane grating. From such an analysis, one can obtain the grating equation, focussing condition and abberations [11, 12]. Diffraction equation of a plane grating is given by

$$N \ m \ \lambda = \cos \alpha - \cos \beta, \tag{22}$$

where α and β are the grazing angle of incidence and diffraction respectively. N is line density, m is the diffraction order and λ is wavelength of light.

Using spherical grating chronological focusing equation of radius R_r [11].

$$\frac{\sin^2 \alpha}{R} - \frac{\sin \alpha}{R_r} + \frac{\sin^2 \beta}{R'} - \frac{\sin \beta}{R_r} = 0 \tag{23}$$

Results of these spherical grating can be applied for plane grating [12] by putting $R_r = \infty$ in Eq. 23, therefore

$$\frac{R'}{R} = -\left(\frac{\sin \beta}{\sin \alpha} \right)^2 \tag{24}$$

Defining C_{ff} as

$$C_{ff} = \left(\frac{\sin \beta}{\sin \alpha} \right) \tag{25}$$

The virtual source distance can then be determined by,

$$R' = -R C_{ff}^2 \tag{26}$$

By fixing the value of C_{ff}, the virtual source distance can be fixed and hence it is called fixed focus constant.

Plane grating magnification is defined as the ratio of size of image S' to the size of the object S and is given by [8]

$$M = \frac{S'}{S} = \frac{R'}{R} \frac{\sin \alpha}{\sin \beta} = -\left(\frac{\sin \beta}{\sin \alpha} \right)^2 \frac{\sin \alpha}{\sin \beta} \tag{27}$$

So, the magnification in terms of C_{ff} is

$$M = -C_{ff} = -\sqrt{\left| \frac{R'}{R} \right|} \tag{28}$$

From the grating Eq. 22, one can see that λ is a function of α and β. Wavelength can be set by choosing arbitrary values of α and β, within the working range of plane grating. However, from the above discussions one can see by choosing arbitrary values of α and β that changes the virtual source distance and the focus arbitrarily. This is

solved by operating the beamline in the fixed focus condition, or equivalently at a fixed C_{ff} or magnification. Furthermore, if the grating is illuminated vertically with collimated light, the beamline can be operated with a free choice of C_{ff}, within the working range of the monochromator [14]. Using the extra constraint of C_{ff} and the grating Eq. 22, the grazing angle of incidence α can be derived to be (see Appendix section B-16)

$$\alpha = \cos^{-1} \frac{-Nm\lambda + \sqrt{1 + C_{ff}^4 + C_{ff}^2((Nm\lambda)^2 - 2}}{C_{ff}^2 - 1} \tag{29}$$

The grazing diffracted angle β can then be obtained using Eq. 25

$$\beta = a\sin(C_{ff} \cdot \sin\alpha) \tag{30}$$

By choosing a value of C_{ff} and and its corresponding α and β, one can then change the wavelength (energy) of the beamline. Any spread or uncertainty in either α or β, ($\Delta\alpha$ or $\Delta\beta$) will change the energy and also the value of C_{ff} and hence contribute to the energy resolution of the beamline. Some of the factors that can cause the spread of α and β are alignment errors, slope errors of the optical elements, vibrations, source size and exit slit opening.

One of the design goals of Bloch beamline was to reach source and the exit slit limited energy resolution [1]. This thesis focuses mainly on contribution to the energy resolution from the finite source size and the exit slit opening. Taking derivative of Eq. 22 with respect to α and β, respectively

$$\frac{\Delta\lambda}{\Delta\alpha} = \frac{\partial\lambda}{\partial\alpha} \quad \text{and} \quad \frac{\Delta\lambda}{\Delta\beta} = \frac{\partial\lambda}{\partial\beta} \tag{31}$$

Therefore,

$$\left(\frac{\Delta\lambda}{\lambda}\right)_\alpha = \left(\frac{\sin\alpha}{m\,G\,\lambda}\right)\Delta\alpha \quad \text{and} \quad \left(\frac{\Delta\lambda}{\lambda}\right)_\beta = \left(-\frac{\sin\beta}{m\,G\,\lambda}\right)\Delta\beta \tag{32}$$

As shown in Figure 15, the variation of the incident angle $\Delta\alpha$ is due to finite source size S and distance R is given by

$$\Delta\alpha = \frac{S}{R} \tag{33}$$

So the contribution to the resolution from the spread in α due to the finite source size is given as

$$\left(\frac{\Delta\lambda}{\lambda}\right)_S = -\frac{\sin\alpha}{m\,N\,\lambda} \cdot \frac{S}{R} \tag{34}$$

The contribution to the resolution from the exit slit size can be mimicked as variation of β due the virtual source size demagnified by the focussing mirror [8]

$$\left(\frac{\Delta\lambda}{\lambda}\right)_{Slit} = \frac{\sin\beta}{m\,N\,\lambda} \cdot \frac{S_{slit}}{R''} \tag{35}$$

19

Energy and wavelength are related by equation,

$$E = \frac{h \cdot c}{\lambda}, \tag{36}$$

where h is Planck's constant and c is velocity of light.

Therefore, the energy resolution is related to variation in wavelength by

$$\left(\frac{\Delta E}{E}\right) = \left(\frac{\Delta \lambda}{\lambda}\right) \tag{37}$$

Finally writing the resolution in terms of energy using Equations 36 and 37, the contribution to the energy resolution from the source size and the exit slit size can be determined as

$$\Delta E_S = \frac{E^2 \sin \alpha}{m \ N \ hc} \cdot \frac{S}{R} \tag{38}$$

$$\Delta E_{Slit} = \frac{E^2 \sin \beta}{m \ N \ hc} \cdot \frac{S_{slit}}{R'} \tag{39}$$

The total energy resolution due the finite source size and the exit slit opening (assuming the uncertainties have Gaussian distribution) can be determined as

$$\Delta E = \sqrt{\Delta E_S^2 + \Delta E_{slit}^2} \tag{40}$$

The electron source size (σ_e) at the center of the undulator is at Bloch beamline is 185 µm x 13 µm (HxV) [15]. Due to diffraction limit, the photon source size will be larger than the electron beam size and with the wavelength. The diffraction limited photon source size (σ_{ph}) is given by $\sqrt{2 * L * \lambda}/2\pi$, where L is the length of the undulator and λ is the wavelength of the photons [13]. Hence, the final source size σ_s would be given as $\sigma_s = \sqrt{\sigma_e^2 + \sigma_{ph}^2}$. For low photon energies σ_e dominates over σ_{ph}. For a photon energy of 21 eV, this value is about 93.6 µm.

The source size and the exit slit size contribution to the energy resolution for C_{ff} = 2.25 and 800 lines/mm for a photon energy of 21 eV, is shown in Figure 16a. The parameters used are undulator length L = 2.8754m, source size σ_s=93.6 µm (Full Width Half Maximum (FWHM) = 220.4 µm), source distance R = 14 m and focussing mirror to the exit slit distance R'=9m. One can see that the energy resolution is dominated by source size for the small slit widths. The total energy resolution for C_{ff} = 2.25 at a photon energy of 21 eV, for 92 and 800 and 2400 lines/mm gratings are shown in Figure 16b. One can see that for the same slit width, the energy resolution is better for higher line density. It is mentioned at Bloch beamline, one cannot reach 21 eV with 2400 lines/mm as the angles required are beyond the allowed range.

(a) (b)
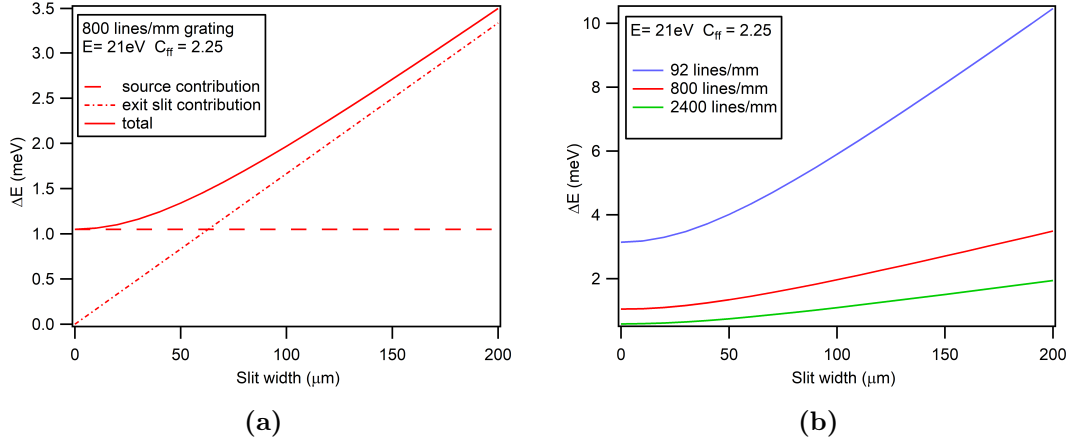
Figure 16: The left panel shows the total energy resolution along with source size, exit slit width contribution for photon energy of 21 eV with 800 lines/mm gratings and C_{ff}=2.25. It is clearly seen that source size contribution dominates and smaller slit widths. The right panel shows the total energy resolution at 21 eV as a function of exit slit width for 92 and 800 lines/mm gratings for C_{ff}=2.25. It is clearly seen that for same exit slit, higher line density has higher resolving power. For both panels, a value of 93.6 μm was used for full width half maximum for the vertical source size (including electron and diffraction limited size).

6.2 Ray tracing method

It is important to double check the results from analytical calculations which have inbuilt simplifications. This is done by performing a rigorous ray tracing method. The ray tracing software used in this work is 'RAY' [7]. This software uses Monte Carlo simulation technique to compute the trajectories of each ray starting from source to each of the optical element (mirror, grating, etc.). Each optical element modify the trajectory of rays. Parameters of the optical elements for ray tracing method are the same as shown in Table 1.
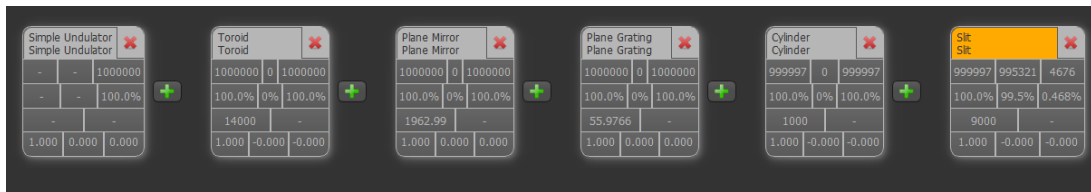
Figure 17: Picture shows beamline set up using Ray tracing software

To find the energy resolution, using this method, the beamline is set up as shown in Figure 17. The orientations of various optical elements are shown in Figure 9. The source is an undulator having length 2.8754 mm producing millions of photon rays with a chosen energy and energy spread. These rays are then incident on a toroidal mirror which focuses the beam horizontally at the exit slit and collimates the beam vertically. Then next is the monochromator which consists of a plane mirror M2 and PG. The software allows

21

one to choose values of C_{ff} and grating line density as required. The energy dispersed rays are then incident on the mirror M3, which focuses the beam vertically at the exit slit. There were no slope errors used for the optical elements. At the exit slit, the beam properties are displayed showing energy distribution, path difference, angular distribution. For example, fixing slit width with a source energy of E = 21 eV and 800 lines/mm, C_{ff} = 2.25 on grating, a trace run produces an image such as shown in Figure 18 having energy resolution ΔE= 1.05 meV. The results of energy resolution (FWHM) at 21 eV for C_{ff} = 2.25, as a function of the exit slit for the three different grating line densities, namely 92, 800 and 2400 lines/mm are shown in Figure 19. The numerical values of the results obtained are shown in Table 4. One can see from Figure 19, that for the same slit width, higher line densities give better energy resolution as one would expect. Also one can notice that the decrease in the energy resolution slows down for smaller slits. This is due to the total energy resolution being dominated by contribution to the energy resolution from the source size compared to contribution from the size of exit slit opening. This was discussed in detail in Section 6.1. The diffraction limited photon source size from the undulator is calculated by the RAY software to be σ = 93 µm which is similar to the value one obtains analytically (see Section 6.1).
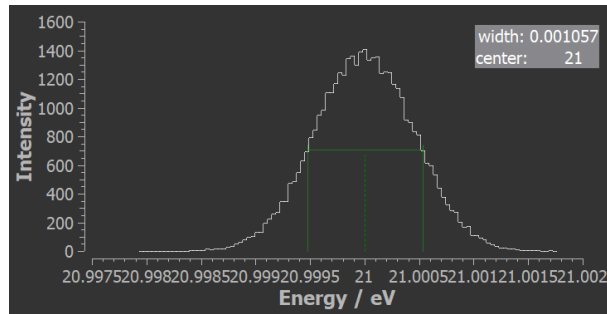
Figure 18: Figure shows energy resolution of 1 meV for slit width of 10 µm on 800 lines/mm, C_{ff} = 2.25.
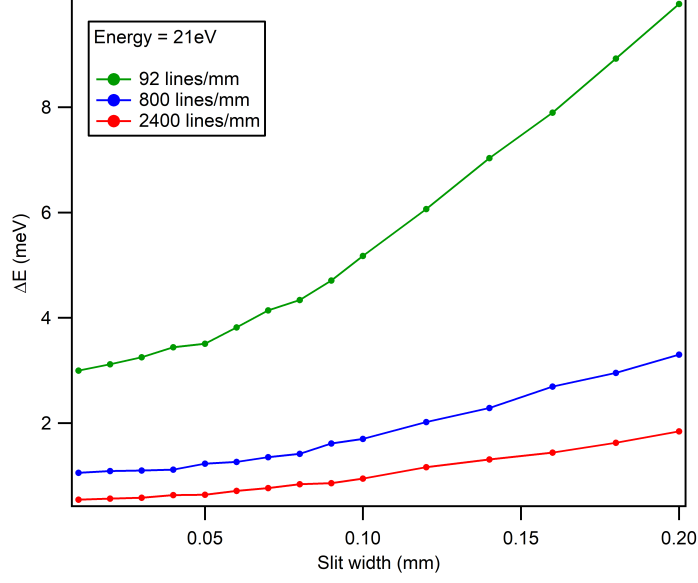
Figure 19: Results of energy resolution at 21 eV as a function of exit slit for 92, 800 and 2400 lines/mm gratings using $C_{ff} = 2.25$. It is clearly seen that for same exit slit, higher line density has higher resolving power.

Table 3: Ray tracing results of slit width versus Energy resolution for the three different gratings using C_{ff}=2.25.

Slit width (mm)	Grating		
	800 lines/mm	92 lines/mm	2400 lines/mm
0.01	1.054	2.9960	0.54480
0.02	1.087	3.118	0.5641
0.03	1.097	3.252	0.5826
0.04	1.114	3.439	0.6329
0.05	1.228	3.507	0.6379
0.06	1.261	3.819	0.7127
0.07	1.353	4.142	0.7661
0.08	1.417	4.339	0.8370
0.09	1.614	4.710	0.8596
0.10	1.698	5.175	0.9468
0.12	2.019	6.067	1.162
0.14	2.285	7.035	1.308
0.16	2.694	7.899	1.439
0.18	2.953	8.924	1.627
0.20	3.300	9.9963	1.844

7 Results and discussion

7.1 Experimental method for grating misalignment

In the beamline, despite best efforts during installation of the gratings, one could still have some roll ϕ and these need to be checked and corrected. There are three different grating with different (92, 800, 2400) lines/mm density as well as M2 mirror in the monochromator. They are kept in ultra high vacuum chamber. From one of the beamline computer, it is possible to change the grating to the required one without disturbing the whole optical system. For roll determination, one can use the zero order configuration, that is grating pitch equal to M2 pitch. For determination of roll, the idea is to maximize the flux measured on a diode placed after the exit slit, by changing the M3 pitch angle for various values of the grating pitch. A plot of M3 pitch versus grating pitch from such a procedure is in Figure 21 as open red circles. One can see that the M3 pitch versus grating pitch is linear. The slope of this line from a linear fit is found to be 0.00911 rad or 9.11 mrad. To determine the roll value, one can use the conclusions reached from a simple analytical model and the ray tracing model, which says that the roll is about 0.9 times the slope of such a plot. The roll misalignment in this case, can then be estimated to be about 8.2 mrad. This roll misalignment was then corrected and data taken again after the correction and is shown as blue open circles. The slope of the linear fit after the roll correction was $-48\,\mu$rad and the corresponding slope is then estimated to be $-43\,\mu$rad. This says that the grating is now well aligned and one can perform the measurements to determine the energy resolution. The data values of the M3 pitch versus grating pitch are shown in Table 4.

(a)   (b)
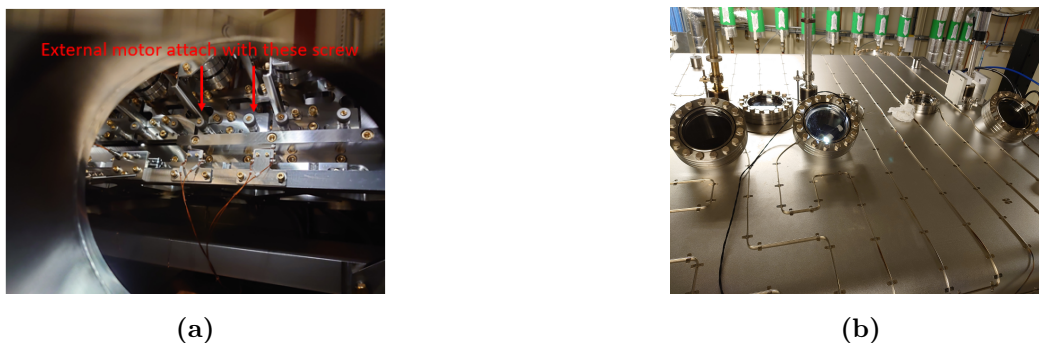
Figure 20: The left panel showing the picture of the alignment screws attached to the grating holder. The right panel showing the picture of screw drivers used for roll and yaw adjustments on grating from outside the chamber.
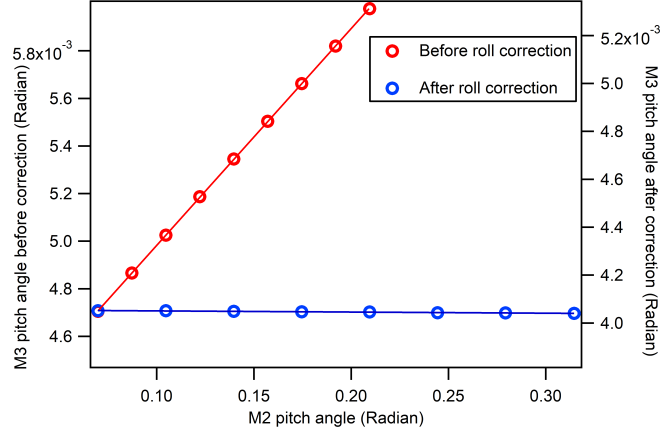
Figure 21: M3 pitch versus grating pitch angle measured by maximizing the photon flux on a diode placed after the exit slit. The open red circles are data taken before the roll correction and the open blue circles are data after the roll correction. The solid red line is a linear fit to the data before roll correction and the solid blue line after the roll correction. The slope before correction was 9.11 mrad and after the correction was $-48\,\mu$rad. Using the results from the ray tracing and the simple analytical model that the roll is 0.9 times the slope. The estimated roll before and after the correction are about 8.2 mrad and $-43\,\mu$rad.

Table 4: Experimental data of M3 pitch versus grating pitch before and after the roll correction.

| Grating pitch angle θ (deg)	Grating pitch angle (rad)	M3 pitch Before correction	M3 pitch After correction
4	0.0698132	0.004705	0.004051
5	0.0872665	0.004866	
6	0.1047198	0.005025	0.004051
7	0.1221731	0.005187	
8	0.1396264	0.005345	0.004049
9	0.1570797	0.005504	
10	0.174533	0.005662	0.004047
11	0.1919863	0.00582	
12	0.2094396	0.005977	0.004046
13	0.2268929		
14	0.2443462		0.004043
15	0.2617995		
16	0.2792528		0.004042
17	0.2967061		
18	0.3141594		0.00404

7.2 Energy resolution

7.2.1 Ion-yield experiment

To avoid any contribution from the grating roll misalignment, all the energy resolution measurements reported in the thesis were done after the grating roll misalignment was corrected.

A schematic view and a picture of the ionization chamber used for performing total ion yield experiment is shown in Figure 22a. The ionization chamber is placed just after the exit slits chamber. The ionization chamber consist of two electrodes, one electrode is a wire which is grounded through picoampere meter to record the ion current. The ion current is in the range of 10^{-15} - 10^{-12} A. The other electrode is in the shape of a half cylinder, to which a positive voltage is applied to repel the positive ions generated towards the wire and to attract the electron created from ionisation. The photons pass just above the wire as shown in the Figure 22a. The gas understudy (He or Ne) is leaked through the leak valve. The gas pressure was $\approx 10^{-3}$ mbar. Various pumps are installed on either side of the ionization chamber, to substantially reduce the pressure increase on either side of the exit slit, that is towards the end station and towards the ring side.

In the ion yield measurements, the photons excite the electron to high Rydberg series levels from which they autoionize to create ions, which is measured as current on the wire.

(a) (b)
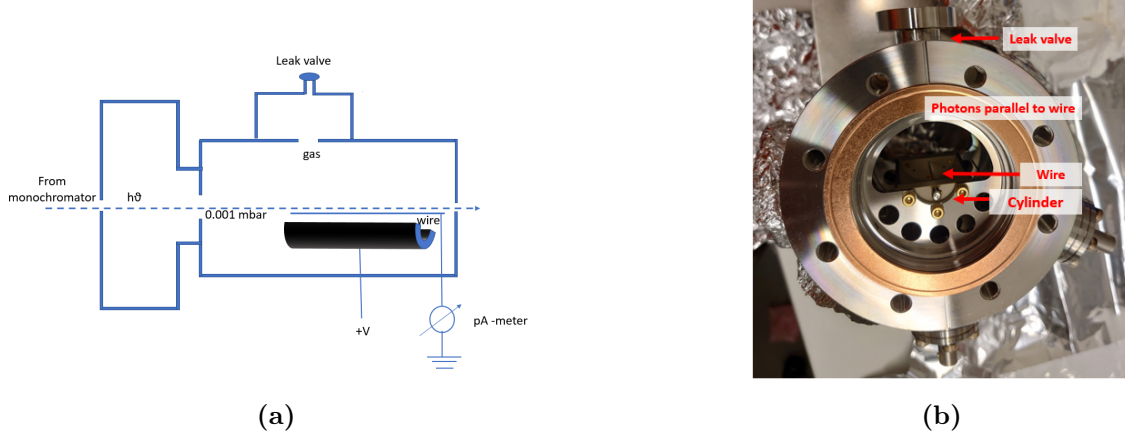
Figure 22: The left panel shows a schematic of gas ionization chamber. The right panel shows the picture gas cell at Bloch beamline.

7.2.2 He- double-excitation spectra

He ion yield spectra were used for estimating the beamline resolution at around 60 eV. Measurements were taken with and without applying positive voltage to the cylinder. The energy resolution with and without the bias were similar for 10 µm slit width, however ion current was higher with a positive bias. All the measurements shown here were taken with a bias voltage of 60 V. After the gas pressure settled to the required value 10^{-3} mbar, the

cold cathode gauge was disabled and the magnet was removed to avoid any effects due to magnetic field from the gauge. The pressure on the gauges are shown in the Figure 23.
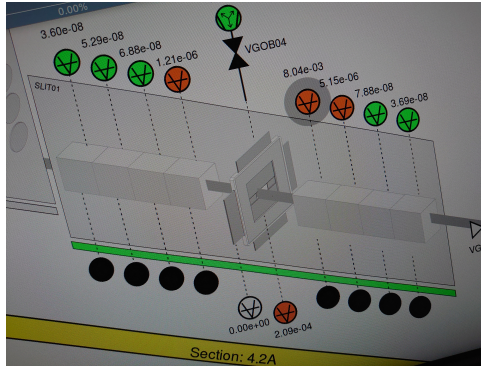
Figure 23: Image shows the pressure on both sides of gas chamber.

The measurements were performed for various slit widths from $10\,\mu m$ to $200\,\mu m$ for both 800 and 2400 lines/mm gratings and C_{ff}=2.25. The spectra for 2400 lines/mm are shown in Figure 25 as red circles.

To estimate the energy resolution, these spectra were fitted using a Fano line shape convoluted with a rounded box function following the procedure described in article [22]. The software program used was IGOR-PRO. The fittings were done using a macro written by Alexander Generalov of MAX IV Laboratory. The fitted spectra for 2400 lines/mm grating is shown in Figure 25a as a solid lines. The resulting energy resolution (FWHM) for various slit width are shown in Figure 25b.
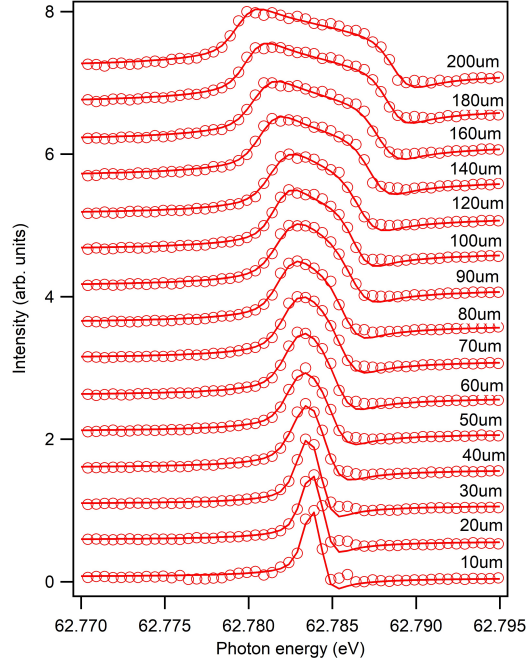
Figure 24: He ion yield spectra along with fit using C_{ff} =2.25 for 2400 lines/mm grating at various exit slit opening. Open red circles are the experimental data. The solid red lines are the fit using Fano line shape convoluted with with a rounded box function.

The results obtained from fitting spectra shown in Figure 24 and similar ones are plotted in , along with results obtained using analytical method and ray tracing model. One can see from Figure 25 that the energy resolution from the analytical method, ray tracing method match closely to the experiments. The energy resolution for the 2400 lines/mm grating is better than 800 lines/mm as expected. Since the simple analytical calculations and a full ray tracing model were done without including any slope errors or instrumental errors, the experimental results, clearly indicate that the beamline energy resolution is solely dependent on the finite source size and exit slit width.

A table of the data obtained from fitting spectra in Figure 24 is shown in Table 5.
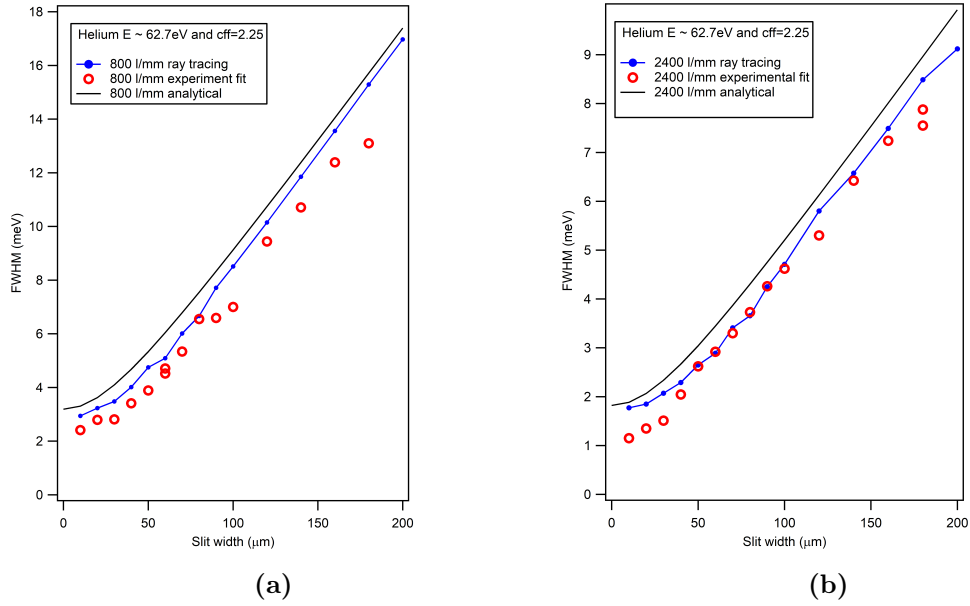
Figure 25: Results of energy resolution at around 62.5 eV as a function of slit width obtained from fitting experimental data similar to Figure 24 (red circles), ray tracing (blue line with dots) and analytical (black line). The left panel are results for 800 lines/mm grating and the right panel for 2400 lines/mm gratings.

Table 5: Table for Helium fitting data

Slit width (µm)	800 lines/mm fitting	2400 lines/mm fitting
10	2.41	1.15
20	2.792	1.35
30	2.81	1.51
40	3.41	2.045
50	3.89	2.62
60	4.52	2.92
70	5.34	3.3
80	6.55	3.73
90	6.59	4.26
100	7	4.62
120	9.44	5.3
140	10.71	4.62
160	12.39	7.24
180	13.1	7.88

7.2.3 Ne ion yield spectra

Neon ion yield spectra was used for measuring the beamline energy resolution at around 21 eV. Similar to He, the Ne pressure was around 10^{-3} mbar. Measurements were taken with and without applying positive voltage to the cylinder. As in the case of He, the energy resolution with and without applying a bias voltage was checked for 10 µm slit width and found to be similar. All the measurements shown here were taken with a bias voltage of 30 V. Similar to the case of He, before the measurements, the cold cathode gauge was disabled and the magnet removed.

The measurements were performed for various slit widths from 10 µm to 110 µm for 800 lines/mm gratings and $C_{ff} = 2.25$. A series of spectra are shown in Figure 26 as open red circles.
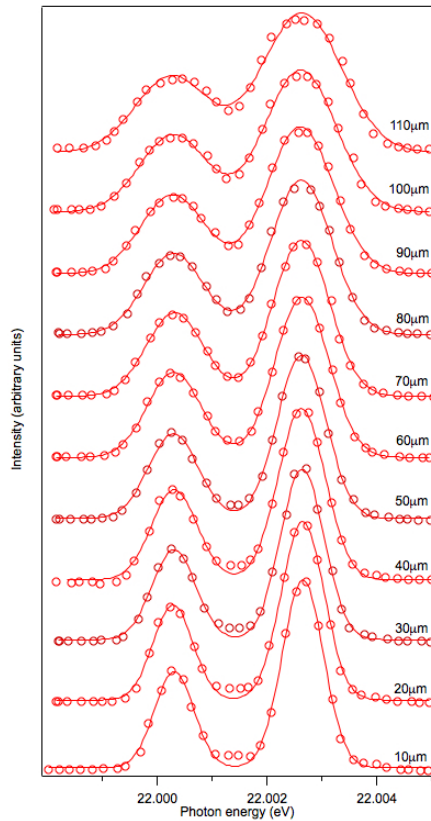
Figure 26: Neon ion yield spectra for various slit width. The red circles are experimental points and the solid lines are from Gaussian fitting.

To estimate the energy resolution, these spectra were fitted in IGOR-PRO software using a Gaussian line shape function (one for each peak). In principle one should use a Lorentzian (for natural line width), convoluted with a Gaussian. However, the procedure is justified as the inherent lorentzian line width are smaller than 50 µeV and the width is to a large extent are dominated by the photon resolution. The fitted spectra for 800 lines/mm grating are shown in Figure 26 as a solid lines. The resulting energy resolution

(FWHM) of the second peak (around 22.003eV) for various slit width are shown in Figure 27 with open red circles. The values obtained from the fittings are shown in Table 6. Also shown in Figure 27 are the results from the ray tracing as green line with dots and from analytical calculations as solid blue line. From the above graph one can see that the ray tracing method fits reasonably well with the experiments.
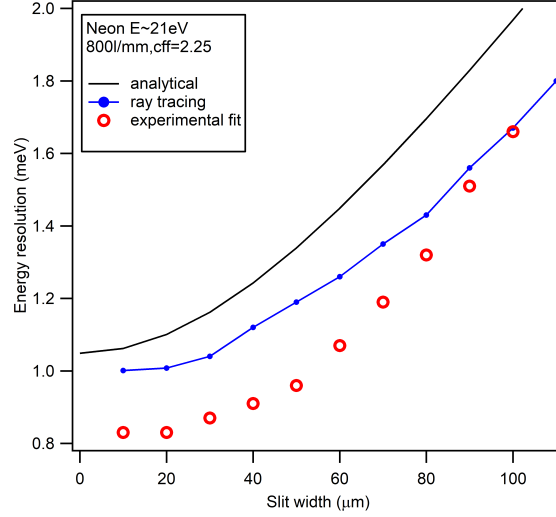
Figure 27: Graph shows the energy resolution using Neon gas as a function of slit width obtained from experiment (red circles), ray tracing (blue line with dots) and analytical (black line) for 800 lines/mm grating.

Table 6: Table for Neon fitting data

Slit width (µm)	800 lines/mm fitting
10	0.83
20	0.83
30	0.87
40	0.91
50	0.96
60	1.07
70	1.19
80	1.32
90	1.51
100	1.66

8   Conclusions

In the first part of the work, grating roll misalignment were investigated using a simple analytical model, ray tracing model and experimental method. The main conclusion from the simple analytical model was that for small angles, the relationship between M3 pitch and grating pitch was proportional to the grating roll misalignment. For the parameters of the Bloch beamline, the grating roll was 0.9 times, the slope of M3 pitch versus grating pitch plot. The results from ray tracing agree well with the simple analytical model. The Experimental data were taken for 800 lines/mm grating, which gave a slope of about 9.1 mrad that corresponds to a roll misalignment of about 8.2 mrad. The roll misalignment was corrected before the energy resolution was measured. In the second part of the work, the energy resolution of the beamline was investigated using a simple analytical model, full ray tracing of the beamline (with only source size and the exit slit width contributions), and experimental method by ion yield measurements. The energy resolution as a function of exit slit width for C_{ff} of 2.25 were done at 21 eV and 62 eV, by using total ion yield measurements of Neon and Helium gas respectively. The energy resolution were found to closely match with ray tracing and analytical methods showing that the Bloch beamline energy resolution is source size and the slit width limited atleast for energies up to 62 eV .

References

[1] R. Sankari, Detailed optical design report, Internal report, MAX IV Laboratory (2012).

[2] S. Mobilio, F. Boscherini, and C. Meneghini, *Synchrotron Radiation: Basics, Methods and Applications* (Springer-Verlag Berlin Heidelberg 2015).

[3] STANDA, `http://www.standaphotonics.com/`.

[4] T. Balasubramanian, B. N. Jensen, S. Urpelainen, B. Sommarin, U. Johansson, M. Huttula, R. Sankari, E. Nõmmiste, S. Aksela, H. Aksela, and R. Nyholm, The normal incidence monochromator beamline i3 on max iii, AIP Conference Proceedings **1234**, 661 (2010).

[5] M. Domke, T. Mandel, A. Puschmann, C. Xue, D. Shirley, G. Kaindl, H. Petersen, and P. Kuske, Performance of the high-resolution sx700/ii monochromator, Review of Scientific Instruments **63**, 80 (1992).

[6] MAX IV, ARPES beamline at Bloch, `https : / / www . maxiv . lu . se / accelerators-beamlines/beamlines/bloch/bloch-beamline-optics/` (2013).

[7] F. Schäfers, *The BESSY Raytrace Program RAY. In A. Erko, M. Idir, T. Krist, and A. G. Michette (Eds.), Modern Developments in X-Ray and Neutron Optics, Volume 137 of Springer Series in optical science, Chapter 2. Berlin, Heidelberg: Springer Berlin Heidelberg.* (2008), pp. 9–41.

[8] W. Grizolli, Optical studies for synchrotron radiation beamlines, Ph.D. thesis, MAX IV Laboratory (2015).

[9] Alisa Danilenko, Alignment correction for plane grating monochromator using the cff parameter,https://www.desy.de/f/students/2017/reports/AlisaDanilenko (2017).

[10] H. Petersen, The plane grating and elliptical mirror: A new optical configuration for monochromators, Optics Communications **40**, 402 (1982).

[11] T. Namioka, Theory of the concave grating. I, J. Opt. Soc. Am. **49**, 446 (1959).

[12] M. V. R. K. Murty, Use of convergent and divergent illumination with plane gratings∗, J. Opt. Soc. Am. **52**, 768 (1962).

[13] H. Onuki and P. Elleaume, eds., *Undulators, wigglers and their applications* (2002).

[14] R. Follath, The versatility of collimated plane grating monochromators, Nuclear Instruments and Methods in Physics Research Section A: Accelerators, Spectrometers, Detectors and Associated Equipment **467-468**, 418 (2001), 7th Int.Conf. on Synchrotron Radiation Instrumentation.

[15] MAX IV, 1.5 GeV storage ring, `https : / / www . maxiv . lu . se / accelerators-beamlines / accelerators / accelerator-documentation / 1-5-gev-storage-ring/` (2013).

[16] J. Bahrdt, Permanent magnets including undulators and wigglers (2011), `arXiv: 1103.1573[physics.acc-ph]`.

[17] H. Petersen, C. Jung, C. Hellwig, W. B. Peatman, and W. Gudat, Review of plane grating focusing for soft x-ray monochromators, Review of Scientific Instruments **66**, 1 (1995).

[18] D. Maystre, Diffraction gratings, http://www.scholarpedia.org/article/Diffraction$_g$ratings.

[19] K. Radler and J. Berkowitz, Photoionization mass spectrometry of neon using synchrotron radiation: Anomalous variation of resonance widths in the noble gases, J. Chem. Phys. **70**, 216 (1979).

[20] T. Namioka, Diffraction gratings, in J. Samson and D. Ederer, eds., *Vacuum Ultraviolet Spectroscopy I* (Academic Press 1998), *Experimental Methods in the Physical Sciences*, volume 31, pp. 347 – 377.

[21] K. Ito, K. Ueda, T. Namioka, K. Yoshino, and Y. Morioka, High-resolution absorption spectrum of Ne in the region of 565–595 Å, J. Opt. Soc. Am. B **5**, 2006 (1988).

[22] M. Hoesch, T. K. Kim, P. Dudin, H. Wang, S. Scott, P. Harris, S. Patel, M. Matthews, D. Hawkins, S. G. Alcock, T. Richter, J. J. Mudd, M. Basham, L. Pratt, P. Leicester, E. C. Longhi, A. Tamai, and F. Baumberger, A facility for the analysis of the electronic structures of solids and their surfaces by synchrotron radiation photoelectron spectroscopy, Review of Scientific Instruments **88**, 013106 (2017).

9   Acknowledgements

A   Appendix

All rotation matrix are along anticlockwise direction. Rotation along Z axis is Yaw rotation.

$$R_z = \begin{pmatrix} \cos\sigma & -\sin\sigma & 0 \\ \sin\sigma & \cos\sigma & 0 \\ 0 & 0 & 1 \end{pmatrix} \tag{1}$$

Rotation along X axis is roll rotation.

$$R_x = \begin{pmatrix} 1 & 0 & 0 \\ 0 & \cos\phi & \sin\phi \\ 0 & -\sin\phi & \cos\phi \end{pmatrix} \tag{2}$$

Rotation along y axis is pitch rotation.

$$R_y = \begin{pmatrix} \cos\theta & 0 & -\sin\theta \\ 0 & 1 & 0 \\ \sin\theta & 0 & \cos\theta \end{pmatrix} \tag{3}$$

Normal N* (0, 0, -1) rotation along X-axis for roll misalignment.

$$R_x \cdot N^* = N_\phi \tag{4}$$

$$\begin{pmatrix} 1 & 0 & 0 \\ 0 & \cos\phi & \sin\phi \\ 0 & -\sin\phi & \cos\phi \end{pmatrix} \begin{pmatrix} 0 \\ 0 \\ -1 \end{pmatrix} = \begin{pmatrix} 0 \\ -\sin\phi \\ -\cos\phi \end{pmatrix} \tag{5}$$

Considering pitch rotation clockwise, then

$$R_Y \cdot N_\phi = \vec{N} \tag{6}$$

$$\begin{pmatrix} \cos\theta & 0 & \sin\theta \\ 0 & 1 & 0 \\ -\sin\theta & 0 & \cos\theta \end{pmatrix} \begin{pmatrix} 0 \\ \sin\phi \\ -\cos\phi \end{pmatrix} = \begin{pmatrix} -\sin\theta\cos\phi \\ -\sin\phi \\ -\cos\theta\cos\phi \end{pmatrix}. \tag{7}$$

B   Appendix

Focus constant and grating equation are

$$C_{ff} = \frac{\sin\beta}{\sin\alpha} \tag{1}$$

and

$$NK\lambda = \cos\alpha - \cos\beta \tag{2}$$

from equation B.1,

$$\sin\beta = C_{ff}\sin\alpha \tag{3}$$

Taking equation B.2,

$$\cos\alpha - \cos\beta = NK\lambda \tag{4}$$

$$(\cos\beta)^2 = (\cos\alpha - NK\lambda)^2 \tag{5}$$

$$\cos^2\beta = \cos^2\alpha - 2NK\lambda\cos\alpha + (NK\lambda)^2 \tag{6}$$

$$1 - \sin^2\beta = \cos^2\alpha - 2NK\lambda\cos\alpha + (NK\lambda)^2 \tag{7}$$

$$\tag{8}$$

substituting equation B.3 , get

$$1 - C_{ff}^2\sin^2\alpha = \cos^2\alpha - 2NK\lambda\cos\alpha + (NK\lambda)^2 \tag{9}$$

$$1 - C_{ff}^2(1 - \cos^2\alpha) = \cos^2\alpha - 2NK\lambda\cos\alpha + (NK\lambda)^2 \tag{10}$$

$$(1 - C_{ff}^2) + C_{ff}^2\cos^2\alpha = \cos^2\alpha - 2NK\lambda\cos\alpha + (NK\lambda)^2 \tag{11}$$

$$(1 - C_{ff}^2) + C_{ff}^2\cos^2\alpha - \cos^2\alpha = -2NK\lambda\cos\alpha + (NK\lambda)^2 \tag{12}$$

$$1 - C_{ff}^2 + (C_{ff}^2 - 1)\cos^2\alpha = (NK\lambda)^2 - 2NK\lambda\cos\alpha \tag{13}$$

re-arranging terms,

$$(C_{ff}^2 - 1)\cos^2\alpha + 2NK\lambda\cos\alpha + (1 - C_{ff}^2 - (NK\lambda)^2) = 0 \tag{14}$$

This is quadratic equation, finding root

$$\cos\alpha = \frac{-2NK\lambda + \sqrt{4(NK\lambda)^2 - 4(C_{ff}^2 - 1)(1 - C_{ff}^2 - (NK\lambda)^2)}}{2(C_{ff}^2 - 1)} \tag{15}$$

$$= \frac{-NK\lambda + \sqrt{1 + C_{ff}^4 + C_{ff}^2((NK\lambda)^2 - 2)}}{C_{ff}^2 - 1} \tag{16}$$

from equation B.2, it is easy to find β angle from α angle (Equations of α and β are derived from [9])

$$\cos\beta = \cos\alpha - NK\lambda \tag{17}$$